

Conversion of waste phosphogypsum into value-added 1D/2D homojunction hydroxyapatite with enhanced structural, morphology, and photoelectrochemical performance

Nur Nabihah Sazali ^a, Mohamad Azuwa Mohamed ^{a,b,c,*}, Siti Fairus Mohd Yusoff ^{a,c}, Nur Shamimie Nadzwin Hasnan ^a, Nurul Atikah Nordin ^a, Nornastasha Azida Anuar ^a, Siti Nurul Falaein Moridon ^{a,b}

^a Department of Chemical Sciences, Faculty of Science and Technology, Universiti Kebangsaan Malaysia, Bangi, Selangor 43600 UKM, Malaysia

^b Fuel Cell Institute, Universiti Kebangsaan Malaysia, Bangi, Selangor 43600 UKM, Malaysia

^c Polymer Research Centre (PORCE), Faculty of Science and Technology, Universiti Kebangsaan Malaysia, Bangi, Selangor 43600 UKM, Malaysia

ARTICLE INFO

Keywords:

Recycling waste
Phosphogypsum
Hydroxyapatite
Surfactant
Photocatalyst
Photoelectrochemical

ABSTRACT

Hydroxyapatite (HAp) as a photocatalytic material has inherent limitations like irregular structure, agglomeration, and a wide band gap, hindering its practical application. In this study, the waste phosphogypsum (PPG) was converted into sustainable HAp with improved photoelectrochemical (PEC) properties via a surface modification strategy by incorporating surfactants like hexadecyltrimethylammonium bromide (CTAB) and non-ionic poly(ethylene glycol)-block-poly(propylene glycol)-block-poly(ethylene glycol) (P123) during hydrothermal synthesis. The addition of CTAB and P123 at varying wt% resulted in diverse HAp morphologies, surface area, light absorption capability, and band gap structure. Also, these modified HAp exhibit improved charge carrier separation due to their enhanced surface areas. Notably, HAp modified with 9 wt% of CTAB as 1D/2D homojunction photocatalyst exhibits a distinct rod-like shape (1D) and flaky (2D) and possesses efficient optoelectronic properties and charge carrier separation. Based on its determined band gap alignment, the resultants HAp can be potentially feasible for various photocatalytic applications.

1. Introduction

Phosphogypsum (PPG) is a solid industrial waste generated during the wet process of producing phosphoric acid from phosphate rock [39]. PPG is primarily composed of gypsum ($\text{CaSO}_4 \cdot 2\text{H}_2\text{O}$), which contains a variety of hazardous impurities such as free phosphoric acid, phosphates, fluorides, and organic matter that adhere to the surface of gypsum crystals and are also substituted in the gypsum crystal lattice [64]. Previous studies have reported that there are 3 tonnes of PPG were produced for every tonne of phosphoric acid produced [39]. Morocco harvests approximately 15 million tonnes of acid PPG residues yearly, most of which are discharged onto land and into the ocean [10]. Only 15 % of global PPG production is used in agriculture, road engineering, cement, and plastering [9]. The remaining 85 % is disposed of without undergoing any additional treatment, which can result in the consumption of significant land resources and the creation of substantial

environmental issues [11]. The production of large quantities of PPG around the world is associated with several environmental concerns such as soil and water contamination. Therefore, converting PPG into a value-added substance like hydroxyapatite (HAp) is a promising strategy for resolving these issues.

HAp with a chemical formula of $\text{Ca}_{10}(\text{PO}_4)_6(\text{OH})_2$ is one of the promising and versatile value-added products which can be converted from PPG waste [56]. HAp is mainly composed of calcium phosphate with morphology and composition similar to human hard tissues such as teeth and bones. Besides, HAp has also been widely used as a catalyst [12], catalyst support [38], biosensor [62], adsorbent for various heavy elements [14], organic dyes [1], and fluoride ions [7]. The nanostructured HAp has multi-adsorbing sites, a large surface area and high biocompatibility due to its similar structure and composition to human bones [71]. HAp is also known as high crystalline nanorods with lengths ranging from 100 to 1000 nm and diameters ranging from 33 to 65 nm

* Corresponding author at: Department of Chemical Sciences, Faculty of Science and Technology, Universiti Kebangsaan Malaysia, Bangi, Selangor 43600 UKM, Malaysia.

E-mail address: mazuwa@ukm.edu.my (M.A. Mohamed).

[39]. Various synthesis techniques have been employed to synthesise HAp, such as solid-state reaction (Javadinejad and Ebrahimi-Kahrizsangi, 2021), co-precipitation (Okuda et al., 2019), the sol-gel process (Türk et al., 2019), hydrothermal process [13], and the microwave synthesis approach (Türk et al., 2017). However, the synthesis of HAp with high surface area has been challenging due to the problem of particle agglomeration, leading to irregularly shaped HAp structures [19]. Long reaction times, agglomeration, uncontrolled particle size, and non-stoichiometric products are drawbacks of these aforementioned synthesis techniques. Among reported synthesis techniques, the hydrothermal method, which can combine moderate temperatures with high pressures, is frequently used to prepare nanocrystalline HAp with controlled size and morphology.

The addition of surfactants has influenced the physical and chemical properties of HAp for applications involving heterogeneous catalysts [51]. The nucleation and growth of HAp crystals can be altered by surfactants, causing the crystals to form in cylindrical, bilayer, or spherical shapes [19]. For instance, a rod-shaped HAp particle resembling bone minerals may be easily manufactured with adjustable sizes using a sufficient concentration of the pluronic acid surfactant (P123) [69]. The rod-shaped HAp demonstrated a greater capacity to load drugs and exhibited improved, sustained drug release characteristics for the negatively charged Bovine serum albumin (BSA) compared to the positively charged and lysozyme (LSZ). The use of surfactants is advocated in other studies for achieving improved control over particle size and morphology (Li Yan et al., 2012; [63]). Previous evidence suggests that the presence of hexadecyltrimethylammonium bromide (CTAB) significantly raised the surface area by up to 3 times, resulting in greater adsorption of CO_3^{2-} ions on its surface compared to the HAp that was synthesised without the use of surfactant [31]. It has been suggested that the powder prepared with surfactant may possess enhanced bioactivity and could be more effective for removing heavy ions prior to undergoing heat treatment. Besides, the 3D hierarchical superstructure of HAp microcrystal morphology was successfully synthesised by adjusting the Ct (trisodium citrate dihydrate)/CTAB ratio and calcium-citrate complex (CC) using hydrothermal treatment [66]. Citrate disrupts the orderly self-assembly of building blocks, and CTAB modifies the development of HAp in an orientation parallel to the C-axis. Nanorod-shaped HAp with a high surface area was successfully synthesized through a hydrothermal process using phosphogypsum waste and potassium dihydrogen phosphate (KH_2PO_4), supplemented with Brij 93 surfactant [7]. XRD analysis confirmed the presence of pure-phase HAp, and SEM and TEM images showed a consistently uniform rod-like structure. This material has valuable uses in catalysis, ion exchange, and gas sensors [7].

CTAB is a cationic surfactant, distinguished by its positively charged quaternary ammonium group. This cationic nature allows it to interact with molecules and surfaces through electrostatic forces. Whereas, P123, is a non-ionic surfactant that has hydrophilic and hydrophobic segments within their molecular structure, enabling them to lower surface tension and stabilize emulsion. CTAB and P123 plays an important role in nanomaterial synthesis where it acts as a surfactant by controlling the particle size, shape and stability during the synthesis. However, up until today the utilization of CTAB and P123 surfactant and its comparison function in the formation of HAp derived from PPG is rarely reported. On top of that, the intricate relationship between the one-dimensional (1D) and two-dimensional (2D) structural and morphological aspects and their impact on the photoelectrochemical (PEC) properties of PPG-derived HAp obtained with either CTAB or P123 surfactant, remains unexplored. Therefore, in this study, we explored the impact of these surfactants and their concentration on the formation of nanostructure PPG-derived HAp by using a simple hydrothermal technique. In this work, the CTAB and P123 surfactant act as a template to control the morphology, size of HAp crystals, and optoelectronic as well as their impact on their PEC properties. This work does not only provide an alternative to recycling PPG waste into a value-

added product but also can be a promising starting material to produce sustainable and low-cost photocatalysts that can be further utilised in a variety of applications such as environmental remediation, water treatment, and energy production.

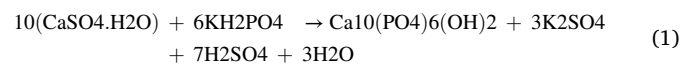
2. Experimental

2.1. Chemicals and materials

The phosphogypsum (PPG) waste samples used in this study were collected from the Malaysian Phosphate Additive Sdn Bhd, a fertiliser industry located in Ipoh, Malaysia. The PPG powders were washed 5 times with distilled water at 80 °C every 30 min to remove the dirt and any impurities, then dried overnight in the oven. Potassium dihydrogen phosphate (KH_2PO_4) as a phosphate source was purchased from Chemiz, sodium hydroxide (NaOH) pellets for pH adjustment were purchased from Bendosen, hexadecyltrimethylammonium bromide (CTAB, $\text{C}_{19}\text{H}_{42}\text{BrN}$) as a cationic surfactant was purchased from Alfa Aesar and the pluronic copolymer (P123, $\text{PEO}_{20}\text{-PPO}_{70}\text{-PEO}_{20}$) as a non-ionic surfactant was obtained from Sigma-Aldrich. All reagents and chemicals were analytical reagent grade, and no purification step was performed.

2.2. Synthesis of PPG-derived HAp

PPG-derived HAp was synthesised by using a hydrothermal technique. Firstly, 2 g of KH_2PO_4 was dissolved in 50 mL of distilled water (DW) under continuous stirring at room temperature. Then, 2 g of pre-washed PPG was added to the KH_2PO_4 solution with continuous stirring at room temperature for 30 min. The solution was adjusted to pH 11 by adding 1 M NaOH solution dropwise. The specific concentration of CTAB and P123 surfactant was added to the mixture and stirred homogeneously at room temperature for 30 minutes. The obtained homogeneous mixture was then transferred into 100 mL Teflon-lined steel autoclaves, tightly sealed and the hydrothermal synthesis was carried out at 180 °C for 15 h. The synthesis products were washed 3 times by centrifugation with distilled water and ethanol in order to remove any impurities. Then, the samples were collected and dried at 70 °C for 24 h in the oven. The resultants PPG-derived HAp with different concentrations of CTAB and P123 surfactant ranging from 3 wt%, 6 wt%, and 9 wt % were denoted as HAp-CTAB-3, HAp-CTAB-6, HAp-CTAB-9, HAp-P123-3, HAp-P123-6, and HAp-P123-9, respectively. The pristine HAp was also prepared with the same procedure without the presence of surfactant during the hydrothermal synthesis. Fig. 1 shows the schematic illustration of the preparation of PPG-derived HAp nanorod. The conversion of PPG waste to HAp was achieved as the chemical reaction below (Eq. 1):



2.3. Characterization methods

Field Emission Scanning Electron Microscope (FESEM) was used to examine the morphology of HAp with different concentrations of surfactant using a Zeiss MERLIN Compact (Zeiss, Germany). Samples were placed on conducting carbon adhesive tapes and then sputtered with a thin layer of platinum to prevent sample charging. The phases and crystallite structure identification of HAp was characterized using a Bruker AXS D8 ADVANCE X-ray diffractometer (XRD)(Bruker, Germany) with $\text{Cu K}\alpha$ radiation. Using an Agilent Technologies Cary 630 instrument, transmission mode was used to capture the spectra in 650–4000 cm^{-1} area. Fourier transform infrared spectrometer (FTIR), was utilised to examine the various functional groups found within both raw PPG and elaborated HAp. Surface area, N_2 adsorption-desorption isotherms as well as pore size distribution and pore volume were

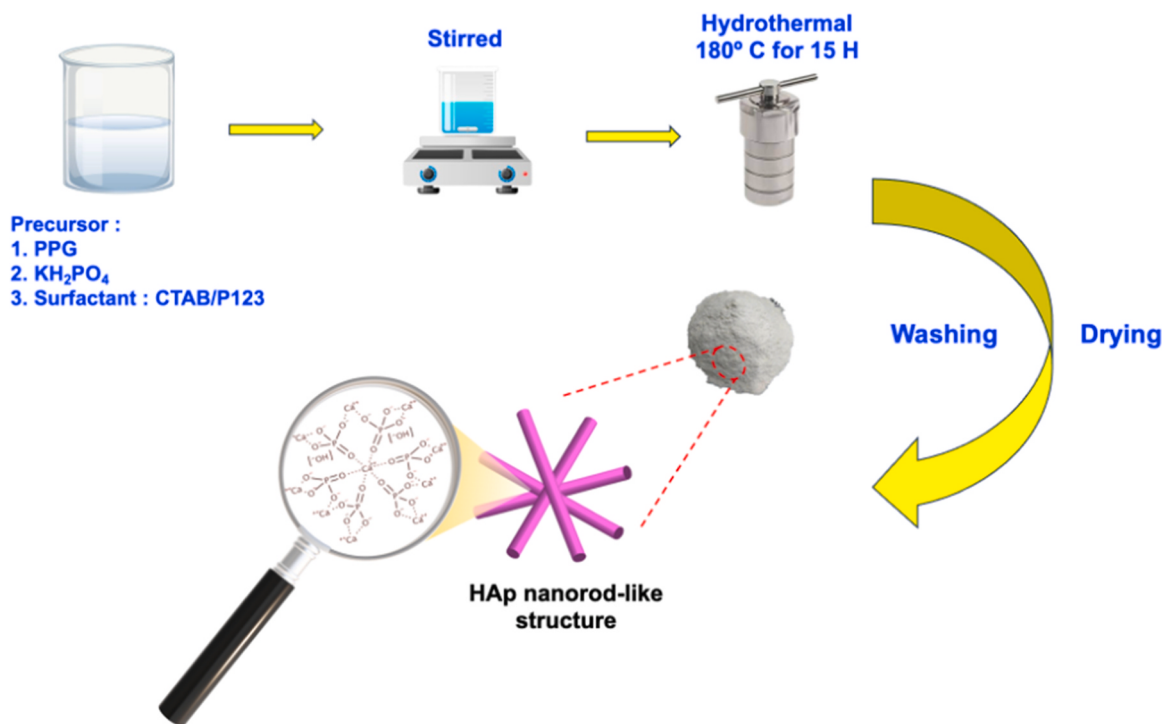


Fig. 1. Schematic illustration of the preparation of nanorod hydroxyapatite.

measured using the Brunauer-Emmett-Teller/Barrett-Joyner-Halenda (BET/BJH) technique in Micromeritics ASAP 2020 Surface Analyzer at -196°C . Prior to analysis, samples were degassed for 3 hours at 300°C under vacuum ($p < 10^{-5}$ mbar). The pore size distribution of the samples was determined using the BJH formula, whereas the specific surface area of the samples was calculated using the BET equation. UV-Vis diffusive reflectance spectroscopy (UV-Vis DRS) at room temperature with a Perkin Elmer Lambda 950 instrument to determine the potential absorption range for each sample. The gathered spectra were transformed into the Kubelka-Munk function, $F(R)$ vs. wavelength. The reflection measurements were then converted to absorption spectra using the Kubelka-Munk transformation (Eq. 2) [46],

$$F(R) = \frac{(1 - R)^{n/2}}{2R} = \frac{K(\lambda)}{S(\lambda)} \quad \propto \alpha = \frac{(hv - E_g)^{n/2}}{hv} \quad (2)$$

where $F(R)$ is the K–M function or re-emission function, R is the diffuse reflectance of an infinitely thick sample, $K(\lambda)$ is the absorption coefficient, $S(\lambda)$ is the scattering coefficient, hv is the photon energy, E_g is the band gap energy, while the value of the integer n depends on the characteristic of optical transition ($n = 1$ or 4 for direct or indirect band transition, respectively). It is commonly accepted that the n value for HAp is 4 [26]. The photon energy, hv , can be calculated using the equation $hv = hc/\lambda$, where h represents Planck's constant (4.136×10^{-15} eV), c stands for the speed of light in a vacuum (2.977×10^{17} nm/s), and λ represents the wavelength (nm). The sample's photoluminescence (PL) spectra were measured using the FLS920 (Edinburgh Instrument) instrument with 350 nm excitation wavelength.

2.4. Photoelectrochemical properties

The photoelectrochemical (PEC) analysis was measured using a potentiostat (Corrtest Instrument, CS Series) with a 3-electrode system PEC cell. The working electrode (1 cm^2 exposed area) was prepared via the doctor-blade coating technique. A 10 mg sample was dispersed in 1 mL of anhydrous ethanol and then evenly ground into a slurry. The slurry was coated onto a clean conductive fluorine-doped tin oxide

(FTO) glass substrate. The prepared sample on FTO was dried for 15 min at ambient temperature and annealed at 350°C for 30 min. The Ag/AgCl electrode and Pt plate (1 cm^2) were used as the reference and counter electrode, respectively, and an aqueous solution of 0.5 M Na_2SO_4 ($\text{pH} = 8$) as the electrolyte. A xenon lamp (Aulight, CEL-TXC250) was a light source under an output intensity of 100 mW cm^{-2} . The transient photocurrent was carried out using the chronoamperometry (CA) technique and was performed with a scan rate of 1 mV/s at a potential of 0.8 V. Mott-Schottky (M-S) analysis was conducted at a frequency of 10 and 100 Hz to determine carrier density (N_D) and flat band (FB). The electrochemical impedance spectroscopy (EIS) was evaluated with AC amplitude at 10 mV, and the frequency ranged from 0.1 Hz and 100 kHz. All the data have been converted to RHE value according to the following equation; $E_{\text{RHE}} = E_{\text{Ag/AgCl}} + 0.05196\text{ pH} + 0.1976$.

3. Results and discussion

3.1. Morphological formation of PPG-derived HAp with surfactant-assisted

The nanoscale morphology and structure of PPG-derived HAp synthesised with and without surfactant were observed using FESEM and TEM analysis. Fig. 2 (a) shows the HAp-CTAB-3 is formed with a shorter nanorod (1D) and flaky structure (2D) and exhibits slight agglomeration. Interestingly, as depicted in Fig. 2 (b) and (c), the presence of flaky HAp structures was not obvious and more well-defined nanorods were formed with the increment of CTAB concentration from 6 wt% (HAp-CTAB-6) to 9 wt% (HAp-CTAB-9), respectively. Besides, the HAp-CTAB-6 and HAp-CTAB-9 samples did not appear severe agglomeration. Similar observations and trends also can be seen in HAp prepared with the presence of P123 surfactant. Contradictory, As shown in Fig. 2 (d), HAp-P123-3 formed a nanorod structure, but it is shorter and has more agglomeration than HAp-CTAB-3. While the prepared samples of HAp-P123-6 [see Fig. 2 (e)] and HAp-P123-9 [see Fig. 2 (f)], appeared to less agglomeration and possessed shorter nanorod structure. The particle size of all HAp samples prepared with the presence of CTAB and P123

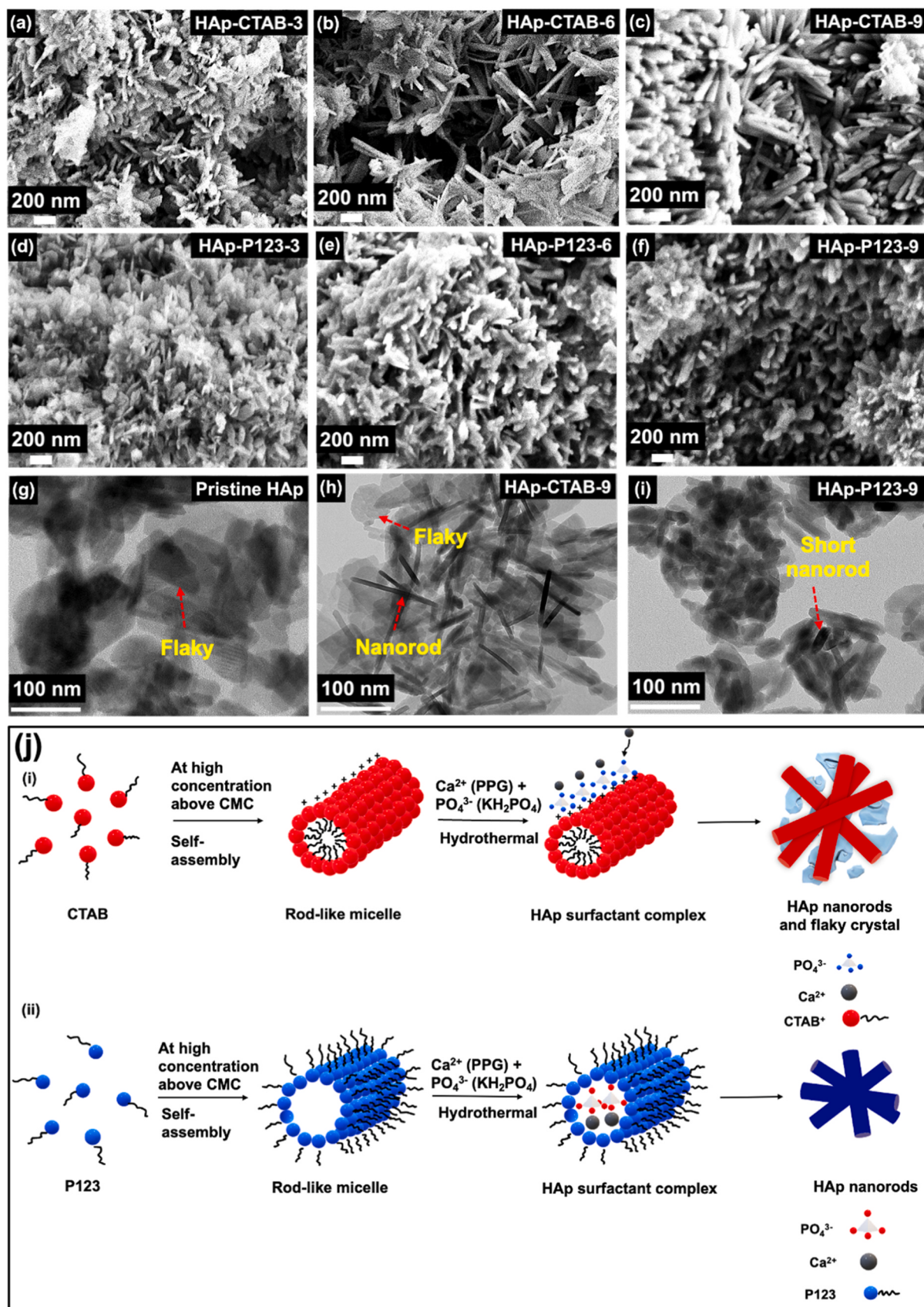


Fig. 2. FESEM micrograph of (a) HAp-CTAB-3, (b) HAp-CTAB-6, (c) HAp-CTAB-9, (d) HAp-P123-3, (e) HAp-P123-6, (f) HAp-P123-9, TEM micrograph of (g) pristine HAp, (h) HAp-CTAB-9, (i) HAp-P123-9, (j) the formation of PPG-derived HAp nanorods in the presence of (i) CTAB and (ii) P123 surfactant.

surfactants was measured and tabulated in Table 1.

As can be observed in Fig. 2 (g), the TEM image of pristine HAp derived from PPG without the presence of either one of the surfactants shows an irregular and flaky shape with obvious agglomerated particles, which is characteristic of its native structure. Based on the more insightful observation via TEM analysis (Fig. 2 (h-i)), it was found that the presence of CTAB and P123 during the hydrothermal process had led to the reduction in flaky HAp formation with more obvious HAp with well-defined nanorods formation. Interestingly, at similar CTAB and P123 surfactant concentrations (9 wt%), the HAp-CTAB-9 exhibits a combination of flaky (2D) and elongated nanorods (1D), while HAp-P123-9 forms shorter nanorods (1D) with the significant disappearance of flaky (2D) structure as demonstrated in Fig. 2 (h) and Fig. 2 (i), respectively. These observations strongly support the conclusion that the introduction of surfactants, both CTAB and P123, has a profound influence on the morphology of the synthesized HAp. The resulting nanorod structures, as revealed by TEM, indicate that surfactants play a crucial role in shaping and directing the growth of HAp particles, leading to the formation of well-defined nanorods.

In comparison with the presence of CTAB, all HAp samples prepared with P123 surfactant exhibited a shorter nanorod even at similar surfactant concentrations. However, the utilization of both surfactants for HAp formation reveals comparable agglomeration occurrence. The difference in terms of size and the occurrence of flaky HAp structure in the prepared samples can be explained based on their difference in chemical structure and properties of the surfactant. A schematic illustration of the CTAB and P123 surfactant as a template for the synthesis of PPG-derived HAp nanorod using the hydrothermal technique is depicted in Fig. 2 (j). Basically, when surfactant molecules dissolve in water, both cationic and non-ionic molecules form structures that minimise their surface tension. The amphiphilic molecules (non-polar hydrophobic region and a polar hydrophilic region) present in the surfactants can adsorb onto the surfaces of particles to lessen interaction between them and regulate the crystal formation [44]. The formation of PPG-derived HAp nanorod with the presence of CTAB surfactant is illustrated in Fig. Fig. 2 j (i). CTAB as a cationic surfactant molecule can be self-assembled into micelles with various shapes when it dissolves in water at a high concentration above critical micelle concentration (CMC). As the concentration of CTAB surfactant in an aqueous medium increases above the CMC concentration, CTAB surfactant micelle assemblies form, functioning as richly positively charged nano-reactors. After the addition of phosphate precursor (KH_2PO_4) into the CTAB surfactant solution, a strong interaction between PO_4^{3-} and CTAB surfactant assemblies occurred due to different electrostatic forces between oppositely charged ions. As soon

as PPG-containing calcium precursors are added, layers of calcium phosphate (CaPO_4) are formed on the surface of surfactant assemblies that contain PO_4^{3-} . These layers are then converted to HAp during the hydrothermal synthesis process. Therefore, it leads to the formation of elongated HAp nanorods as proved by TEM analysis. However, as can be seen in TEM images [Fig. 2 (h)], the HAp-CTAB-9 nanostructures are mainly composed of nanorod-like structures (1D) and flaky-like (2D) crystal structures. This might be due to 9 wt% of CTAB is not the optimum concentration for HAp to fully form a nanorod structure. These results agree with the findings of other studies in which the rod-shaped micelles were formed by a surfactant concentration of 10 wt% [70]. The micelle provides a nucleation site for the surfactant to induce the HAp particle's orientational growth.

On the other hand, like CTAB, at a high concentration above the CMC, P123 can also self-assemble into micelles as can be seen in Fig. 2 j (ii). However, the presence of P123 as a surfactant during hydrothermal synthesis resulted in shorter PPG-derived HAp nanorods compared to PPG-derived HAp obtained with the presence of CTAB surfactant, as confirmed by FESEM and TEM analyses. The P123 surfactant, which consists of a hydrophilic polyethylene oxide (PEO) and a hydrophobic polypropylene oxide (PPO) block is introduced into the HAp synthesis solution. It attaches to the surface of HAp crystals with the PPO block oriented towards the crystal surface of HAp, while the PEO block faces outward. This is due to PEO has a stronger attraction to water compared to PPO, and this difference can impact the surface properties and growth kinetics of HAp crystals. Initially, Ca^{2+} ions bind to the hydrophilic headgroup on the inner surface of micelles through hydrogen bonds, followed by the binding of PO_4^{3-} ions to form layers of HAp. As HAp grows within the P123 micelles, it tends to grow more slowly along the c-axis, leading to the formation of shorter nanorods.

Overall, the HAp-CTAB-9 exhibits a combination of flaky (2D) and elongated nanorods (1D) where the 1D structure attaches parallelly to the 2D structure with good intimacy and interfacial contact as can be seen in Fig. 2(h). The in-situ growth of the 1D and 2D structure of HAp-CTAB-9 which possesses identical composition chemically led to the formation of 1D/2D homojunction photocatalyst, which is beneficial for high-performance HAp photocatalyst. In comparison with heterojunction photocatalyst, it has been suggested that the 1D/2D homojunction photocatalyst significantly demonstrates high efficiency in photoinduced charge transfer and hinders of recombination of charge carriers due to their structure, design, and intrinsic properties [24].

Table 1

Average particle length, crystallinity, BET surface areas, mean pore size, and pore volume of PPG-derived HAp samples with different surfactants and concentrations.

| Samples | Average particles length (nm) ^a | Crystallinity (%) ^b | Average crystallites size (nm) ^c | [Ca] / [P] ratio ^d | BET surface area (m ² /g) | Mean pore size (nm) | Pore volume (cm ³ /g) |
|--------------|--|--------------------------------|---|-------------------------------|--------------------------------------|---------------------|----------------------------------|
| Pristine HAp | 149.2 | 56.7 | 24.5 | 1.78 | 61.78 | 22.61 | 0.39 |
| HAp-CTAB-3 | 219.9 | 61.6 | 24.9 | 1.86 | 61.29 | 23.62 | 0.39 |
| HAp-CTAB-6 | 497.2 | 64.7 | 25.2 | 1.88 | 112.01 | 21.06 | 0.63 |
| HAp-CTAB-9 | 522.5 | 66.3 | 25.7 | 2.04 | 136.01 | 20.65 | 0.75 |
| HAp-P123-3 | 212.9 | 58.6 | 18.3 | 1.84 | 71.24 | 22.12 | 0.43 |
| HAp-P123-6 | 320.2 | 61.7 | 21.5 | 1.94 | 74.27 | 27.23 | 0.50 |
| HAp-P123-9 | 366.7 | 64.3 | 22.57 | 2.13 | 232.57 | 21.95 | 1.51 |

^a Measured from FESEM images using image J software.

^b Estimated from XRD data using Eq. 2.

^c Estimated from XRD data using Eq. 3.

^d Data obtained from EDX analysis.

3.2. Crystallinity and phase analysis

XRD analysis was employed to study the phase and crystalline structure of the prepared HAp samples. The XRD pattern obtained for the PPG and PPG-derived HAp with different types of surfactant and concentration is shown in Fig. 3. The phase composition of PPG is shown in detail in Fig. 3 (a), which the majority composed of calcium sulphate, $\text{CaSO}_4 \cdot 2 \text{H}_2\text{O}$ and SiO_2 . Similar observations also can be found elsewhere [16,18]. As can be seen in Fig. 3 (b), all prepared samples portrayed the identical XRD pattern, which can be observed at 20 of 25.9°, 31.8°, 32.9°, 34°, 39.8°, 46.7° and 49.7° that corresponds to the (002), (211), (300), (202), (310), (222) and (213) crystallographic planes, respectively. The presence of these XRD peaks demonstrated that all prepared PPG-derived HAp possessed high purity of HAp with a hexagonal unit cell lattice (PDF 00-009-0432), with no presence of other impurities crystalline phase. The degree of crystallinity (X_c) of the prepared samples was estimated using the following Eq. (3) [29]:

$$X_c = 1 - \frac{V_{112/300}}{I_{300}} \quad (3)$$

where the $V_{112/300}$ is the intensity of the hollow between (112) and (300) reflections and I_{300} is the intensity of (300) reflection. The degree of crystallinity (X_c) is a critical parameter that quantifies the proportion of a material's structure exhibiting a crystalline arrangement. As tabulated in Table 1, it shows a clear trend in the degree of crystallinity for the prepared samples where pristine HAp exhibits the lowest degree of crystallinity at 56.7 %, indicating a substantial presence of amorphous regions within the structure. As CTAB and P123 surfactants are introduced, a gradual increase in crystallinity is observed with increasing surfactant concentration. The highest degree of crystallinity among the

prepared samples is exhibited by HAp-CTAB-9 suggesting a more ordered and crystalline structure in HAp. This is due to the adsorption of surfactant onto the surface of HAp that can modify the crystal growth and orientation of the HAp nanoparticles, leading to changes in the crystallinity of the prepared sample. The interaction between surfactant and HAp can result in the formation of a more ordered structure, with a higher degree of crystallinity, due to the preferential adsorption of surfactant molecules onto specific crystal facets [25].

The average crystallite size (D) of the prepared samples was estimated by using Scherrer equation:

$$D = \frac{K\lambda}{\beta \cos\theta} \quad (4)$$

where K is Scherrer constant (usually 0.89), λ is the x-ray radiation wavelength ($\text{Cu K}\alpha = 0.15406 \text{ nm}$), β is the line broadening at full width at half maximum (FWHM) in radians, and θ is Bragg diffraction angle in radian, with half of 20. Based on Table 1, the $[\text{Ca}]/[\text{P}]$ ratio of prepared HAp increases with the increment of both CTAB and P123 surfactants from 3 wt% to 9 wt%. Besides, an increase in both surfactant concentrations led to an increment in the degree of crystallinity of the HAp-prepared samples. A stoichiometric HAp has an ideal $[\text{Ca}]/[\text{P}]$ ratio of 1.67 and is often associated with the ideal crystalline structure of HAp. However, in this finding, the crystallinity and $[\text{Ca}]/[\text{P}]$ ratio of all prepared samples steadily increase. In alignment with the finding of Jr et al., an increase in the degree of crystallinity indicates a closer match to the stoichiometric ratio (1.67) which promotes greater structural order and crystallinity [29]. However, our findings indicate a contrasting result, this might be due to surfactants acting as a template to control the size and nucleation growth of nanorod HAp. In summary, both surfactants promote a higher $[\text{Ca}]/[\text{P}]$ ratio for the formation of

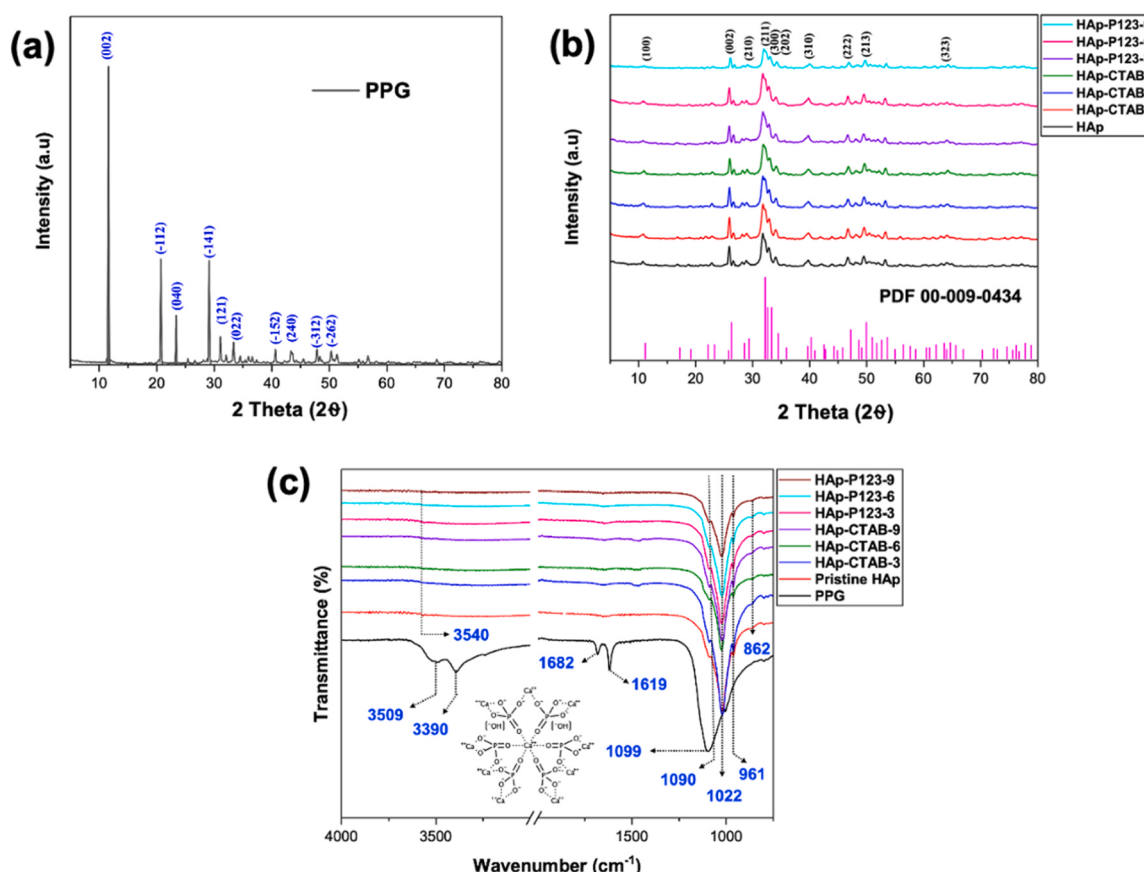


Fig. 3. XRD pattern of (a) PPG and (b) PPG-derived HAp with and without the presence of surfactants, (c) FTIR spectra PPG-derived HAp with and without the presence of surfactants.

PPG-derived HAp with significant improvement in phase formation, crystallinity and crystallite size.

The lattice spacing (d) of the prepared samples was estimated by using Bragg's equation:

$$n\lambda = 2dsin\theta \quad (5)$$

where n is the order of diffraction ($n = 1$), d is the lattice spacing of the crystal lattice, λ is the x-ray radiation wavelength ($Cu\text{ K}\alpha = 0.15406\text{ nm}$), and θ is Bragg diffraction angle in radian, with half of 2θ . The calculated lattice spacing of all prepared samples is determined to be 0.344 nm and 0.281 nm at (002) and (211) planes, respectively. The similar lattice spacing value of all samples indicated that the presence of surfactant during HAp formation does not significantly disrupt the HAp crystal's lattice. This finding is consistent with previous literature (Li Yan et al., 2012; [48,63]), where the surfactant-assisted method only affects the morphology and surface properties of HAp.

3.3. Chemical composition and chemical formation analysis

FTIR spectroscopy analysis was employed to further confirm the successful conversion of waste PPG into PPG-derived HAp samples with different surfactants and various concentrations. As displayed in Fig. 3 (c), the FTIR spectra of the PPG sample exhibited the water's stretching and bending vibrational modes, which were observed in the region of $3509\text{--}3390\text{ cm}^{-1}$ and $1682\text{--}1619\text{ cm}^{-1}$, respectively. The sharp and intense absorption bands at 1099 cm^{-1} are associated with the asymmetric stretching vibrational sulfate groups SO_4^{2-} of PPG. Interestingly, the absorption band characteristic sulfate groups SO_4^{2-} of PPG is absent in FTIR spectra of PPG-derived HAp synthesized with and without CTAB and P123 surfactants. This observation strongly suggested that the PPG has been fully converted into HAp under hydrothermal synthesis conditions. The appearance of a broad FTIR band centred around $1000\text{--}1100\text{ cm}^{-1}$ is an indication of the formation of HAp [34]. The peak at 962 cm^{-1} is associated with the P-O bond in the phosphate group's non-degenerate symmetric stretching mode, ν_1 [6]. Another significant peak is observed at around 1022 and 1090 cm^{-1} , which corresponds to the triply degenerate asymmetric stretching mode ν_3 of the P-O bond [3,20,27,28,35,40,49,60,67]. The peak observed at 3540 cm^{-1} is attributed to two specific vibrational modes in the hydroxyl group within the crystal structure of HAp. These modes correspond to the libration (a rocking or swaying motion) and the intramolecular stretching of the hydroxyl group, respectively. This particular peak is also linked to the stretching motion of free O-H bonds, which may be found on the surface of the crystallite [30]. On top of that, a reduction in intensity was observed at 3540 cm^{-1} , corresponding to oxygen vacancies and loss of an OH^- ions. Furthermore, a decrement in the peak intensity related to PO_4^{3-} ions at wavenumbers 962 , 1022 , and 1099 cm^{-1} was also observed with increment of surfactant concentration, indicating a reduction in oxygen. This observation also supported by a decrease in the atomic composition of oxygen, as evidenced in the EDX analyses presented in Tables 2 and 3. The band at 862 cm^{-1} is associated with the vibrational modes of CO_3^{2-} ions. The presence of these distinct bands implies that the PO_4^{3-} groups in the HAp lattice have undergone a partial substitution by CO_3^{2-} groups [52]. This substitution most likely occurred due to the capture of atmospheric carbon dioxide

Table 3

Estimated band gap, valence band edge, conduction band edge values and oxygen wt% of prepared HAp.

| Sample | Band gap (eV) | E_{VB} (eV) | E_{CB} (eV) | Concentration of O (wt %) ^a |
|-------------|---------------|---------------|---------------|--|
| HAp | 3.46 | 2.31 | -1.15 | 44.0 |
| HAp-CTAB-3% | 3.42 | 2.29 | -1.13 | 41.0 |
| HAp-CTAB-6% | 3.41 | 2.29 | -1.12 | 38.5 |
| HAp-CTAB-9% | 3.40 | 2.28 | -1.12 | 34.1 |
| HAp-P123-3% | 3.28 | 2.22 | -1.06 | 36.4 |
| HAp-P123-6% | 3.21 | 2.19 | -1.02 | 34.1 |
| HAp-P123-9% | 3.19 | 2.17 | -1.04 | 29.4 |

^a Data obtained from EDX analysis.

during the preparation process. In general, the FTIR analysis demonstrated a commendable concordance with the XRD analysis, affirming the successful acquisition of PPG-derived HAp in the hydrothermal synthesis process, irrespective of the specific surfactants employed.

3.4. Surface composition analysis

The XPS analysis was employed to gain a further understanding of the surface chemical state and chemical composition of the prepared samples. As depicted in Fig. 4 (a), the full survey spectra of the HAp-CTAB-9 sample showed the existence of typical elements in HAp such as calcium (Ca), phosphorus (P), oxygen (O) and carbon (C), which is consistent with those reported in the literature [53,55]. The nitrogen (N) and bromine (Br) elements were not detected, confirming the absence of CTAB ($C_{19}H_{42}BrN$) impurities in the HAp-CTAB-9 sample. This observation is also consistent with FTIR analysis and further supports the conclusion that the CTAB has most likely been washed away during sample preparation. The high-resolution spectra of Ca 2p, P 2p, O 1s, and C1s were precisely fitted to confirm the formation of chemical bonding in the HAp-CTAB-9 sample.

As depicted in Fig. 4 (b), the high-resolution Ca 2p spectra of HAp-CTAB-9 show an obvious doublet band which has been fitted into four main peaks at 347.3 , 350.6 , 349.1 and 352.6 eV . The first prominent peak observed at a binding energy of 347.3 eV corresponds to the Ca $2p_{1/2}$ orbital, which indicates the presence of Ca-O bonds in HAp, such as Ca-O and Ca-OH [42]. While, the peak at 350.6 eV is attributed to the Ca $2p_{3/2}$ region, representing the calcium phase on HAp [33]. The fitted peaks at 349.1 eV is assigned to the Ca- CO_3 bond for the partially substitution of PO_4 with CO_3 due to adsorption of atmospheric carbon dioxide, while 352.8 eV is corresponded to Ca^{2+} ions, which represent the oxidation state of calcium in HAp. Dreghici et al., [15].

As depicted in Fig. 4 (c), the high-resolution P 2p spectra of HAp-CTAB-9 can be fitted into three prominent peaks at 133.6 , 134.7 , and 136.4 eV . The fitted peaks located at 133.6 and 134.7 eV are attributed to $2p_{3/2}$ and $2p_{1/2}$, which are associated with P-O bonding of phosphate group (PO_4) and P-O bonding in P_2O_5 , respectively [42]. Whereas, the peak fitted at 136.4 eV corresponds to the oxidation state of PO_4^{3-} ions in

Table 2

FTIR adsorption bands for the functional groups of PPG-derived HAp samples with different surfactants and concentrations.

| Peak assignments | Observed vibrational frequencies (cm^{-1}) | | | | | | |
|--------------------------------------|---|-------------|------------|------------|------------|------------|------------|
| | Pristine HAp | HAp- CTAB-3 | HAp-CTAB-6 | HAp-CTAB-9 | HAp-P123-3 | HAp-P123-6 | HAp-P123-9 |
| ν_1 stretching mode, PO_4^{3-} | 961 | 961 | 957 | 961 | 961 | 963 | 961 |
| ν_3 stretching mode, PO_4^{3-} | 1021–1088 | 1019–1088 | 1023–1088 | 1023–1088 | 1025–1088 | 1025–1088 | 1023–1088 |
| Stretching mode, OH | 3540 | 3540 | 3540 | 3540 | 3540 | 3540 | 3540 |
| ν_2 bending mode, CO_3^{2-} | 862 | 862 | 862 | 862 | 862 | 862 | 862 |

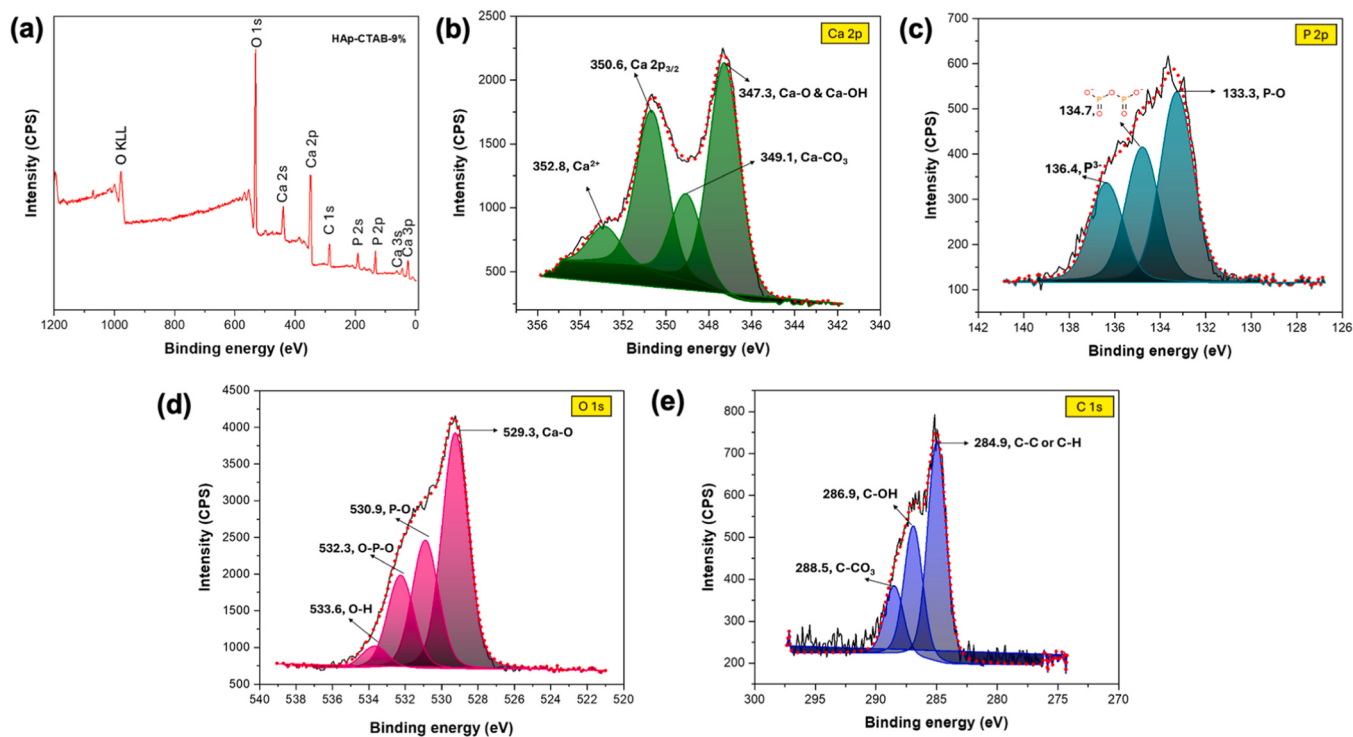


Fig. 4. (a) XPS full survey spectra and XPS high-resolution spectra of (b) Ca 2p, (c) P 2p, (d) O 1s and (e) C 1s of HAp-CTAB-9 sample.

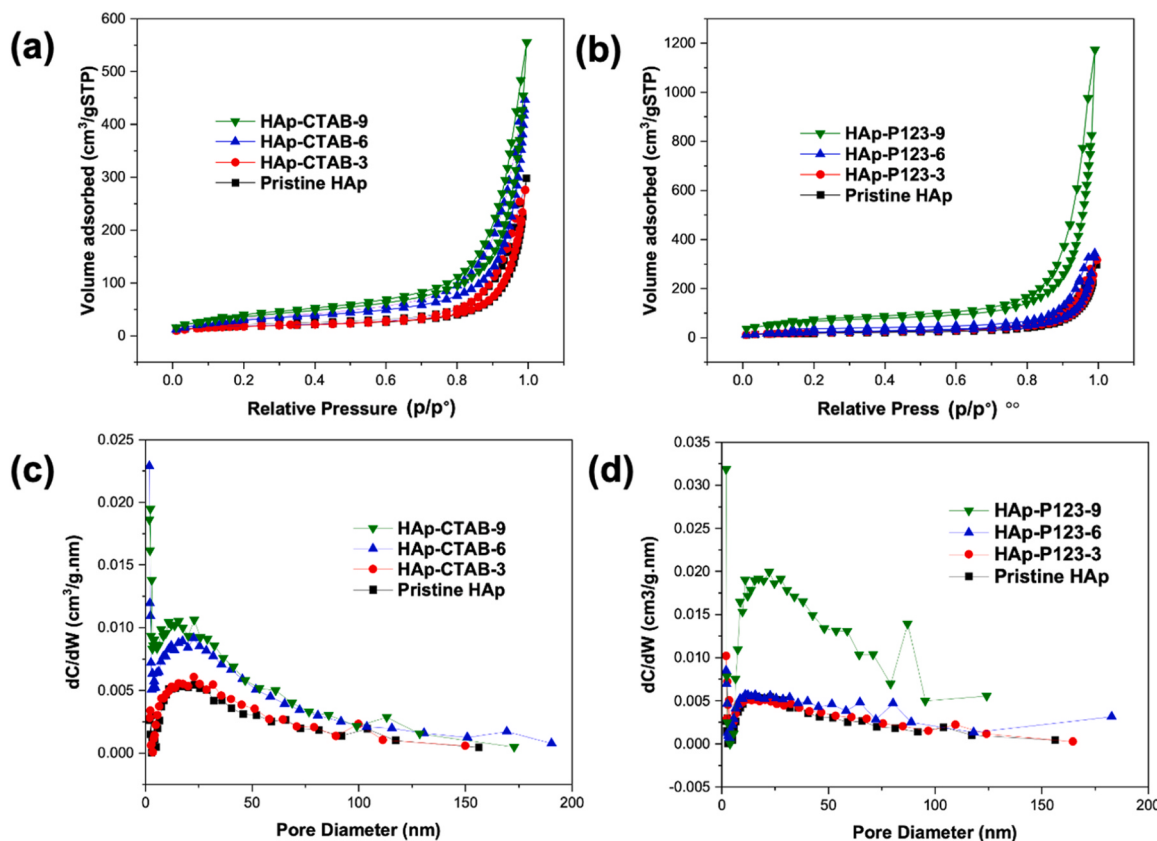


Fig. 5. N₂ adsorption-desorption isotherms of the as-prepared (a) HAp, HAp-CTAB-3, HAp-CTAB-6, HAp-CTAB-9, (b) HAp, HAp-P123-3, HAp-P123-6, HAp-P123-9 and corresponding pore distribution plots of prepared samples (c) HAp, HAp-CTAB-3, HAp-CTAB-6, HAp-CTAB-9 and (d) HAp, HAp-P123-3, HAp-P123-6, HAp-P123-9.

HAp (Yan He and Shuang Men, 2020). The high-resolution O 1 s spectra in Fig. 4 (d) exhibit four major peaks upon fitting. The fitted peak at 529.3 eV, 530.9 eV, 532.3 eV, and 533.6 eV can correspond to the Ca-O bond, P-O bond, O-P-O bond, and the O-H bond of adsorbed H₂O, respectively [4]. As can be observed, the peaks representing P-O bond, O-P-O bond, and the O-H bond in the spectrum appear notably diminished compared to the Ca-O bond peak. This difference suggests the presence of oxygen vacancies within the HAp. Further evidence comes from the decreased intensity of PO₄³⁻ and OH⁻ ions in the FTIR analyses, as well as a lower concentration of oxygen detected in the EDX analyses.

In Fig. 4 (e), the high-resolution C 1 s spectra with binding energies of 284.8, 286.9, and 288.5 eV. The primary peak corresponds to the typical C-C bond or C-H bond of adventitious carbon species or surface contamination by atmospheric organic carbon. The second peak corresponds to the C-OH of the hydroxyl group (OH) [17]. Additionally, the peak at 288.3 eV indicates the presence C-O in the carbonate ion (CO₃) adsorbed in HAp [4]. In conclusion, the observed peaks validate the successful conversion of PPG to HAp. This outcome aligns with the findings from the FTIR analysis, which also indicate the presence of all these corresponding bonds.

3.5. Surface area and porosity analysis

The impact of type and various concentrations of surfactants on the

textural characteristics of the synthesised PPG-derived HAp was further elucidated using N₂ adsorption-desorption isotherms analysis. The BET surface area, mean pore size and pore volume are tabulated in Table 1. The curves [Fig. 5(a-b)] showed that overall N₂ sorption isotherms for both surfactants are typical for type IV with steep H3 hysteresis loop in relative pressure of (P/P₀) range of 0.8–1.00, further validating the existence of mesoporous features [59]. The textural characteristics of pristine HAp were obtained with a specific surface area of 61.78 m²/g with a mean pore size of 22.61 nm (see Table 1).

As compared to pristine HAp, all prepared samples with different types and concentrations of surfactant exhibit higher surface areas, especially HAp-CTAB-9 and HAp-P123-9. However, interestingly, HAp-CTAB-9 has a lower BET surface area of 136.01 m²/g, along with a mean pore size of 20.65 nm, in contrast to HAp-P123-9, which has a surface area of 232.57 m²/g and a mean pore size of 21.95 nm. This lower BET surface area typically corresponds to larger particle sizes as confirmed by XRD analysis (see Table 1). Additionally, as the concentration increased, all prepared samples exhibit a continued increment in surface area. Other research conducted by Hajermia et al. and Nga et al. has shown that HAp-P123 has a high surface area due to its micelle shape and size [19,48]. Specifically, P123 micelles have larger sizes when compared to CTAB because P123 is composed of a triblock copolymer with PEO and PPO blocks. Whereas, CTAB consists of a long hydrocarbon chain and a positively charged quaternary ammonium group.

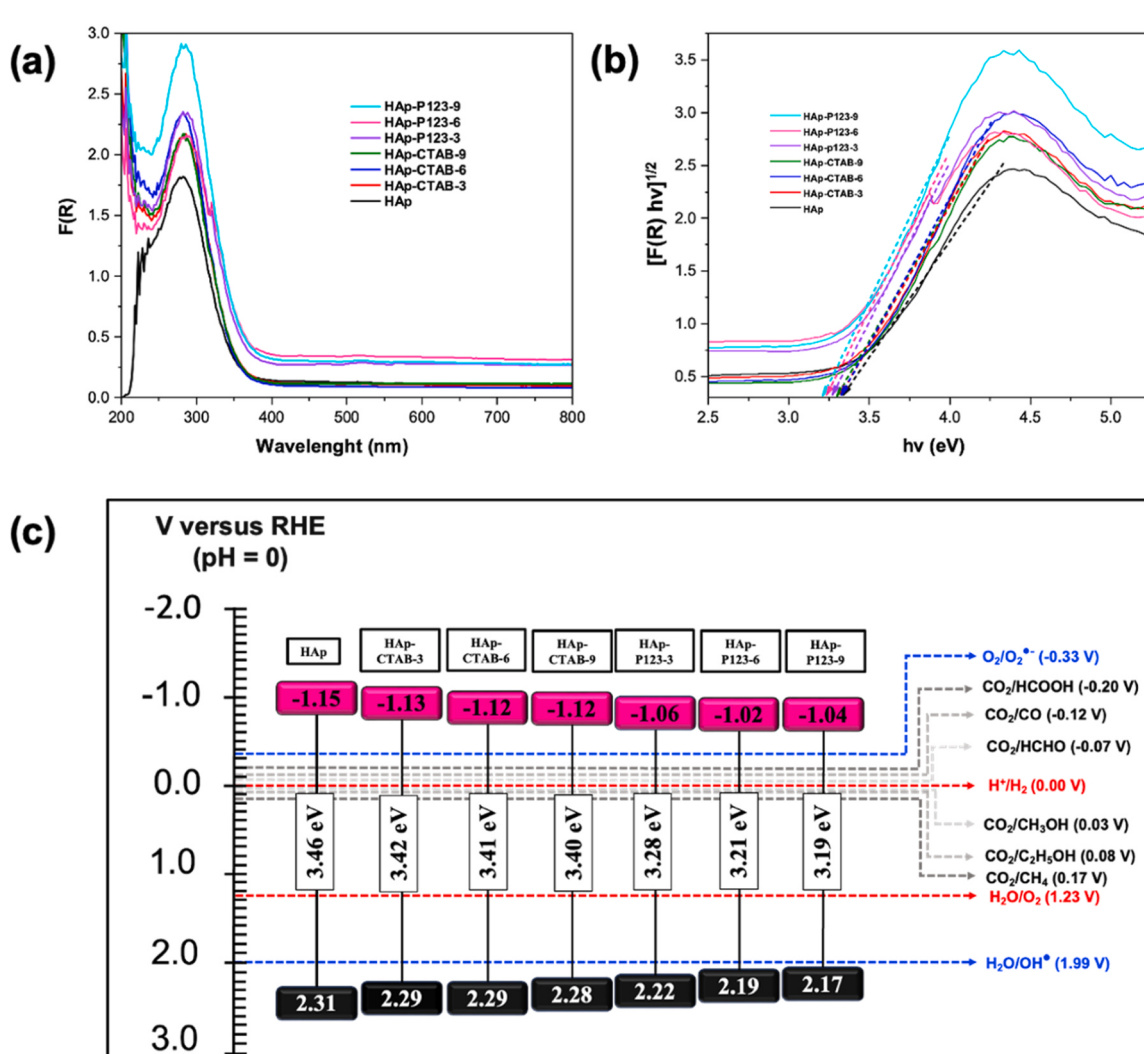


Fig. 6. (a) Kubelka-Munk optical absorption curve of prepared samples (b) band gap determination of prepared samples (c) Band gap alignment of prepared HAp samples.

Although CTAB can also self-assemble into micelles in water, these micelles are typically more spherical in shape and smaller in size than P123 micelles. Kuperkar et al., [32].

3.6. Optical properties analysis

UV-Vis DRS spectroscopy analysis was used to investigate the effect of type and various concentration of surfactants on the optical properties of the prepared PPG-derived HAp samples. The Kubelka-Munk curves and band gap determination for each sample were depicted in Fig. 6 (a) and (b), respectively. All the PPG-derived HAp samples displayed the same optical absorption capacity which mainly absorbs light irradiation in the UV region (200 – 370 nm). The presence of CTAB and P123 surfactants does not significantly enhance the HAp's ability to absorb visible light, however, the peak intensity of all sample increases as the concentration of the surfactant increases. It seems possible that these results are due to the enhancement of light scattering, as the crystallinity of the HAp prepared sample with surfactants increases, as confirmed by XRD results. The optical band gap energies of the HAp prepared samples have been obtained using the Kubelka-Munk theory from the diffuse reflectance data as illustrated in Fig. 6 (b) and tabulated in Table 2. The energy needed to form electron-hole pairs is known as the optical band gap energy, and it can be used to assess the material composition and the interface between HAp and surfactant (Nimmy and Wilson, 2019b; [57,

61]). As can be observed, the extrapolation on the x-axis gave the estimated value of the optical energy band gap of pristine HAp which was found to be 3.46 eV. Overall, the optical band gap energy of HAp prepared samples with surfactant shows a decrement from 3.42 to 3.19 eV as the concentration of surfactant increases. Additionally, it is observed that the optical band gap energies of the HAp prepared samples with both surfactants are lower than pristine HAp, which can be attributed the existence of oxygen vacancies within the HAp structure, as confirmed by FTIR, XPS, and EDX analysis.

Moreover, the effects of surfactants on the band gap structure were further elucidated by determining the position of their band gap edges. Mulliken electronegativity theory can be used to determine the prepared sample's conduction band (CB) and valence band (VB) edge positions. The CB and VB position was determined by using the following Eqs. (6–7) [23] [45]:

$$E_{VB} = X - E_e + 0.5E_g \quad (6)$$

$$E_{CB} = E_{VB} - E_g \quad (7)$$

E_{CB} and E_{VB} are the conduction band and the valence band relative to the normal hydrogen electrode (NHE), E_g is the band gap energy of photocatalyst, E_e is the energy of free electrons (4.5 eV) and X is the electronegativity of semiconductor (X value for HAp is 5.08 eV). The direct band gap plot revealed small significant differences in band

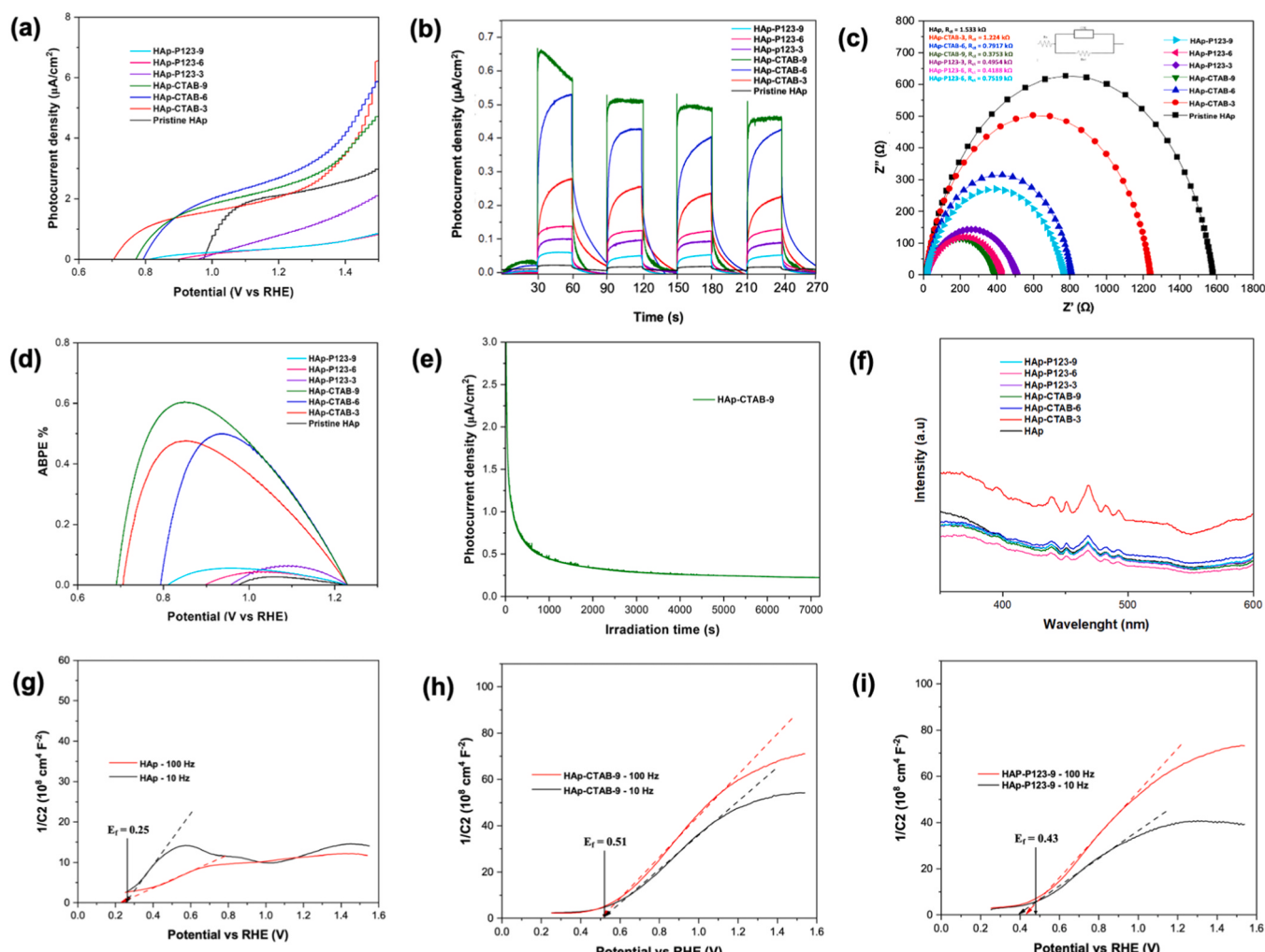


Fig. 7. (a) Photocurrent density measurement measured by linear sweep voltammetry (LSV), (b) transient photocurrent responses, (c) electrochemical impedance spectroscopy analysis, (d) applied bias photon-to-current efficiency (ABPE) % curve all prepared samples (e) photocurrent response stability of HAp-CTAB-9 under long time light irradiation (f) photoluminescence spectra of all prepared samples and Mott Schottky plots of (g) pristine HAp (h) HAp-CTAB-9 and (i) HAp-P123-9.

energies. As illustrated in Fig. 6 (c), the band gap alignment of prepared pristine HAp, HAp-CTAB, and HAp-P123 samples are straddle between redox potentials of water-splitting for hydrogen production and CO₂ photoreduction. the band gap structures of all these samples encompass the necessary for photocatalytic water-splitting and CO₂ [2,21,22].

3.7. Photoelectrochemical performances of PPG-derived HAp

The photocurrent density versus the applied potential in linear sweep voltammetry (LSV) mode of all samples is depicted in Fig. 7 (a). The photocurrent density plot revealed all prepared samples exhibit positive curves, suggesting all prepared samples are n-type semiconductors with electrons as the majority carriers. The photocurrent density plot also revealed that the HAp-CTAB sample exhibited the highest improvement in photocurrent density followed by HAp-P123 and pristine HAp. Besides, in comparison with pristine HAp and HAp-P123, the photocurrent onset potential of all HAp-CTAB samples significantly shifted to lower cathodic potential suggesting the greater ability in water oxidation promoter (Hisatomi et al., 2011). Furthermore, the HAp-CTAB-6 and HAp-CTAB-9 exhibited comparable highest photocurrent density of 2.5 and 2.7 μA cm⁻² at (1.23 V vs. RHE), respectively followed by HAp-CTAB-3, pristine HAp, HAp-P123-3, HAp-P123-6, HAp-P123-9.

In Fig. 7 (b), the transient photocurrent responses of the HAp samples are presented over five on-off intermittent irradiation cycles. As anticipated, the pristine HAp exhibited the lowest photocurrent response due to the rapid recombination of photo-generated electrons and holes. Among the HAp prepared samples, the highest photocurrent intensity was observed in the HAp-CTAB-9 sample, followed by HAp-CTAB-6, HAp-CTAB-3, HAp-P123-6, HAp-P123-3, and HAp-P123-9. The structural modifications introduced by both surfactants resulted in a significant improvement in the separation of photoinduced electron-hole pairs, as evidenced by the higher transient photocurrent response compared to pristine HAp. The increased of photocurrent corresponds to enhanced photocarrier separation efficiency. Furthermore, HAp prepared samples with surfactant exhibited a consistent and repeatable photocurrent response when exposed to visible light, indicating excellent photoelectrochemical stability. Therefore, these findings suggest that a well-defined structure of HAp may possess enhanced light absorption properties, which, when exposed to light can lead to increased photocurrent generation. This is further supported by TEM images, which reveal that HAp samples prepared with 9 wt% of CTAB surfactants exhibit 1D and 2D structures. The combination of 1D/2D materials, such as nanorods and nanosheets, offers a larger exposed surface area, facilitating photon absorption and potentially resulting in higher photocurrent responses. Moreover, the HAp-CTAB-9 sample, with its larger surface area, high crystallinity and diverse facets along with a combination of 1D/2D structures, enables the trapping and scattering of incident photons. This, in turn, results in multiple interactions and enhances light absorption.

To further confirm, EIS was also conducted in order to examine the efficiency of the charge carriers conductivity. The Nyquist plot in Fig. 7 (c) provides valuable information, where a smaller diameter of the semicircle indicates reduced charge transfer resistance, corresponding to lower resistance in charge migration. It was observed that HAp-CTAB-9 exhibited the smallest semicircle diameter compared to pristine HAp and other prepared samples, indicating the lowest electron transfer resistance and highest electrical conductivity. On top of that, as fitted in Fig. 7 (c), the charge transfer resistances (R_{ct}) of pristine HAp, as well as with the addition of CTAB and P123 are 1.533 kΩ, 1.224 kΩ, 0.7917 kΩ, 0.3753 kΩ, 0.4954 kΩ, 0.4188 kΩ, and 0.7519 kΩ, respectively. Based on charge transfer resistances (R_{ct}), HAp-CTAB-9 have the smallest internal resistance among the prepared samples, suggesting a superior transport and separation efficiency for its internal carriers [37]. This finding aligns well with the transient photocurrent responses analysis. For HAp-CTAB-9, the existence of multiple pathways for charge transport, along with well-connected 2D structures, leads to reduced

resistance and facilitates electron transport, with these 2D sheets serving as effective conductive networks. In contrast, HAp-P123-9 features nanorods that provide a distinct electron transport pathway. This suggests that PPG-derived HAp with the CTAB surfactant demonstrates superior performance in electron migration and charge separation, boasting the lowest electron-transfer resistance and high electrical conductivity.

The applied bias photon-to-current efficiency (ABPE) % is determined using the following Eq. (8) [37,47]:

$$\text{ABPE \%} = [J_p(E_0 \text{ rev} - E_{app})/I_0] \times (100) \quad (8)$$

where J_p is the photocurrent density (μA/cm²), I₀ is the illumination intensity (100 mW/cm²), E₀ rev is the standard reversible potential for RHE (1.23 V), and E_{app} is the applied potential. As shown in Fig. 7 (d), HAp-CTAB-9 have the highest ABPE % of 0.60 %, followed by HAp-CTAB-6, HAp-CTAB-3, HAp-P123-3, HAp-P123-9, HAp-P123-6 and pristine HAp at 0.49 %, 0.47 %, 0.06 %, 0.05 %, 0.04 %, and 0.02 %, respectively. These findings suggest that HAp-CTAB-9 demonstrates superior photoinduced electron-hole pair generation [36,45]. On top of that, the photocurrent density stability of HAp-CTAB-9 was tested as depicted in Fig. 7 (e). At initial stage, photocurrent density of HAp-CTAB-9 shows a significant change, dropping from 3.91 μA/cm² to 0.33 μA/cm². Following that, the photocurrent stabilizes, reaching 0.22 μA/cm² after 2 hours. The initial drop in photocurrent density may be attributed to material degradation potentially caused by the detachment of photocatalyst particles following prolonged immersion [37].

Photoluminescence was conducted to study the HAp prepared samples's trapping, migration and electron-hole pair recombination. The semiconductor would emit photons that resulted in photoluminescence due to electron-hole pair recombination after the semiconductor was irradiated. As seen in Fig. 7 (f), the pristine HAp exhibits a higher distinct emission band than other HAp prepared samples with surfactants. This is explained by the electron-hole pair's attraction to one another in their bound state, which leads to the high peak intensity that is attributed to the electron-hole pair's rapid recombination. The decrement in peak intensity of HAp prepared sample with both surfactants also might be due to the high porosity which led to a low charge recombination rate, as confirmed by BET analyses. Furthermore, according to the data tabulated in Table 2, there is a decrease in the concentration (wt%) of oxygen as the concentration of surfactant increases. Notably, HAp-P123 9 % exhibits the lowest concentration of oxygen among the prepared sample. Surface oxygen vacancies play a crucial role as both photoinduced charge traps and adsorption sites. They facilitate the transfer of charges and prevent the recombination of photogenerated charge carriers. This results in an enhanced photocatalytic performance. On the other hand, bulk oxygen vacancies merely function as traps for charge carriers, causing the recombination of photogenerated electron-hole pairs [5,43,58]. Hence, this might be the reason P123 surfactant exhibited poor PEC performance compared to CTAB.

The Mott-Schottky (M-S) equation is typically used to estimate the flat band (E_{fb}) and majority charge carrier density of a semiconductor. The majority charge carrier refers to the type of charge carriers that are present in the higher abundance. The carrier dominates the electrical conduction behaviour of the material and is responsible for carrying the electric current in a material [54]. The carrier density (N_D) can be determined by the slope of M-S curves using the following Eq. (9) [65]:

$$N_D = \left(\frac{2}{e\epsilon\epsilon_0 A^2} \right) \left[\frac{d\left(\frac{1}{C^2}\right)}{dE} \right]^{-1} \quad (9)$$

where $\frac{d\left(\frac{1}{C^2}\right)}{dE}$ is the slope of the tangent line in the Mott-Schottky plot, e is

the electric charge, ϵ is the dielectric constant of the HAp, ϵ_0 is the vacuum permittivity, A is the surface area of the HAp on FTO thin film electrode. Fig. 7 (g), (h) and (i) illustrate the Mott-Schottky plot of pristine HAp, HAp-CTAB-9 and HAp-P123-9 at frequencies of 10 and 100 Hz, respectively. As can be observed, all samples indicated an n-type characteristic with a positive slope which indicates the majority of charger carriers are electrons and the flow of electric current is due to the movement of electrons. HAp has an ϵ value of 15.4, the calculated N_D shows that HAp-CTAB-9 have a high carrier density (N_D) with 6.2017×10^{28} , followed by HAp-P123-9 and pristine HAp with 5.5599×10^{28} and 1.0328×10^{28} , respectively. The flat band potential information can be acquired by extrapolating the linear region of the plots to the potential axis. In comparison to V vs RHE, the E_{fb} for pure HAp is found to be 0.25 V, whereas HAp-CTAB-9 and HAp-P123-9 shifted to 0.51 and 0.43 V, respectively. The negative shift of flat band potential reveals a larger accumulation of electrons and reduced recombination of electrons and holes in the HAp prepared sample with both surfactants [41]. The flat band potential of HAp-CTAB-9 is more negative than other prepared samples due to different morphology and effective homojunction structure of between HAp 1D (nanorod) and HAp 2D (nanosheet).

As confirmed by FTIR analyses, the presence of O vacancies on the O-H group of HAp creates a deep and strong series of energy levels. These energy levels play an important role in the trapping and recombination of electrons and holes [8]. First, light is absorbed by HAp 1D to produce holes and electrons on its surface. The photogenerated electrons from HAp 1D are captured by HAp 2D and play a crucial role in separating the photogenerated charge pairs due to the presence of oxygen vacancies in the O-H and P-O functional group. The presence of oxygen vacancies on the {001} plane facilitates the transfer of photogenerated electrons from HAp 1D under light irradiation. When HAp 2D is exposed to visible light, it generates both holes and electrons, owing to its semiconducting properties. These photogenerated electrons and holes are preferentially accumulated on the {001} and {010} crystal facets, respectively. This accumulation results in the separation of these photoinduced charges across the surface of HAp 2D. At the {001} facet of HAp, oxygen vacancies are formed under light irradiation and acted as capturing photogenerated electrons for more production of activated radicals [50]. These oxygen vacancies sites act as traps for oxygen, and the photogenerated electrons on the HAp 2D surface react with adsorbed oxygen molecules. The transferred electrons and photogenerated electrons on the nanoplates can be transported to a conductive substrate. This transport process helps to suppress the recombination rate of photogenerated charge carriers [68].

This observation suggests that when a surfactant is introduced into HAp, it leads to a combination of a 1D/2D structure. This combination works to reduce the recombination of electrons and holes at the interface. As a result, the decreased recombination of these charges promotes better charge transfer properties at the interface, ultimately enhancing the overall photoelectrochemical (PEC) efficiency of the HAp sample prepared with both surfactants. Furthermore, the increase in the flat band potential provides further support for the improvements seen in photocurrent and electrochemical impedance spectroscopy (EIS) results.

4. Conclusion

In summary, we successfully synthesized nanorod-shaped hydroxyapatite (HAp) structures from waste phosphogypsum (PPG) using CTAB and P123 surfactants as templates via the hydrothermal technique. These surfactants effectively controlled particle morphology and minimized agglomeration, with HAp-CTAB-9 exhibiting a rod-like structures (1D) and flaky-crystal-like structures (2D) due to CTAB's capping action on HAp crystal surfaces. However, surfactant modification had a limited impact on HAp's optical properties. Kubelka-Munk analysis showed no significant peak shifts compared to pristine HAp, however, it did enhance the intensity of UV absorption. This is consistent with HAp's

inherent wide bandgap, predominantly absorbing UV light due to electronic transitions. Nonetheless, the addition of surfactants did enhance HAp's electronic properties to some extent. Photocurrent measurements indicated higher values for HAp-CTAB, especially at higher concentrations of surfactant, suggesting a good photocarrier separation efficiency. Nyquist plots revealed that HAp-CTAB-9 exhibited the lowest resistances, reflecting improved electron-transfer properties and electrical conductivity, favorable for electron migration. Mott-Schottky analysis unveiled variations in flat band potentials among the samples, indicating differences in electronic properties and charge transfer behavior and HAp-CTAB showed the most promising charge transfer potential. Therefore, this work evaluates the use of surfactant to alter HAp to develop high-performance and low-cost photocatalysts

CRediT authorship contribution statement

Mohamad Azuwa Mohamed: Writing – review & editing, Visualization, Validation, Supervision, Data curation, Conceptualization, Funding acquisition, Methodology, Resources. **Siti Fairus Mohd Yusoff:** Writing – review & editing, Validation, Supervision. **Nur Nabihah Sazali:** Writing – original draft, Visualization, Validation, Methodology, Formal analysis, Data curation, Investigation. **Nurul Atikah Nordin:** Writing – review & editing, Visualization, Investigation. **Nornastasha Azida Anuar:** Writing – review & editing, Investigation, Methodology. **Nur Shamimie Nadzwin Hasnan:** Writing – review & editing, Investigation. **Siti Nurul Falaein Moridon:** Writing – review & editing, Investigation, Visualization.

Declaration of Competing Interest

The authors declare that they have no known competing financial interests or personal relationships that could have appeared to influence the work reported in this paper.

Data Availability

No data was used for the research described in the article.

Acknowledgement

The authors gratefully acknowledge the financial support from the UNESCO under the PhosAgro/UNESCO/IUPAC Grants for Research Projects in Green Chemistry (Project Number: ST-2022-001)/(Contract Number: 4500461757) and the authors would also like to acknowledge technical and management support from the Centre for Research and Instrumentation (CRIM) at the Universiti Kebangsaan Malaysia.

References

- [1] A.N. Amenaghawon, C.L. Anyalewechi, H. Darmokoesoemo, H.S. Kusuma, Hydroxyapatite-based adsorbents: applications in sequestering heavy metals and dyes, J. Environ. Manag. 302 (2022) 113989, <https://doi.org/10.1016/j.jenvman.2021.113989>.
- [2] N.A. Anuar, M.A. Mohamed, N.S.N. Hasnan, W.N.A. Wan Mokhtar, M.N. I. Salehmin, L.J. Minggu, M.S. Mastuli, M.B. Kassim, Porous architecture photoelectrode with boosted photoelectrochemical properties for solar fuel production, Int J. Hydron. Energy 51 (2024) 476–507, <https://doi.org/10.1016/j.ijhydene.2023.10.098>.
- [3] I.H. Arita, V.M. Castano, D.S. Wilkinson, Synthesis and processing of hydroxyapatite ceramic tapes with controlled porosity, J. Mater. Sci. Mater. Med. 6 (1995) 19–23, <https://doi.org/10.1007/BF00121241>.
- [4] A. Amedlous, O. Amadine, Y. Essamlali, K. Daanoun, M. Aadil, M. Zahouily, Aqueous-phase catalytic hydroxylation of phenol with H_2O_2 by using a copper incorporated apatite nanocatalyst, RSC Adv. 9 (2019) 14132–14142, <https://doi.org/10.1039/c9ra02021g>.
- [5] X. Bai, L. Wang, R. Zong, Y. Lv, Y. Sun, Y. Zhu, Performance enhancement of ZnO photocatalyst via synergic effect of surface oxygen defect and graphene hybridization, Langmuir 29 (2013) 3097–3105, <https://doi.org/10.1021/la4001768>.

- [6] F. Bakan, O. Laçin, H. Sarac, A novel low temperature sol-gel synthesis process for thermally stable nano crystalline hydroxyapatite, *Powder Technol.* 233 (2013) 295–302, <https://doi.org/10.1016/j.powtec.2012.08.030>.
- [7] H. Bensalah, M.F. Bekheet, S. Alami Younssi, M. Ouamoum, A. Gurlo, Hydrothermal synthesis of nanocrystalline hydroxyapatite from phosphogypsum waste, *J. Environ. Chem. Eng.* 6 (2018) 1347–1352, <https://doi.org/10.1016/j.jece.2018.01.052>.
- [8] V.S. Bystrov, C. Piccirillo, D.M. Tobaldi, P.M.L. Castro, J. Coutinho, S. Kopyl, R. C. Pullar, Oxygen vacancies, the optical band gap (Eg) and photocatalysis of hydroxyapatite: Comparing modelling with measured data, *Appl. Catal. B* 196 (2016) 100–107, <https://doi.org/10.1016/j.apcatb.2016.05.014>.
- [9] Q. Chen, Q. Zhang, A. Fourie, C. Xin, Utilization of phosphogypsum and phosphate tailings for cemented paste backfill, *J. Environ. Manag.* 201 (2017) 19–27, <https://doi.org/10.1016/j.jenvman.2017.06.027>.
- [10] Y. Chernysh, O. Yakhnenco, V. Chubur, H. Roubík, Phosphogypsum recycling: A review of environmental issues, current trends, and prospects, *Appl. Sci.* 11 (2021) 1–22, <https://doi.org/10.3390/app11041575>.
- [11] A.A. Cuadri, F.J. Navarro, M. García-Morales, J.P. Bolívar, Valorization of phosphogypsum waste as asphaltic bitumen modifier, *J. Hazard Mater.* 279 (2014) 11–16, <https://doi.org/10.1016/j.jhazmat.2014.06.058>.
- [12] Q. Cui, S. Chao, Z. Bai, H. Yan, K. Wang, L. Yang, Based on a new support for synthesis of highly efficient palladium/hydroxyapatite catalyst for ethanol electrooxidation, *Electrochimica Acta* 132 (2014) 31–36, <https://doi.org/10.1016/j.electacta.2014.03.129>.
- [13] S.H. Daryan, A. Khavandi, J. Javadpour, Surface engineered hollow hydroxyapatite microspheres: Hydrothermal synthesis and growth mechanisms, *Solid State Sci.* 106 (2020) 106301, <https://doi.org/10.1016/j.solidstatesciences.2020.106301>.
- [14] L. Dong, Z. Zhu, Y. Qiu, J. Zhao, Removal of lead from aqueous solution by hydroxyapatite/manganese dioxide composite, *Front Environ. Sci. Eng.* 10 (2016) 28–36, <https://doi.org/10.1007/s11783-014-0722-5>.
- [15] D.B. Dreghici, B. Butoi, D. Predoi, S.L. Iconaru, O. Stoican, A. Groza, Chitosan-hydroxyapatite composite layers generated in radio frequency magnetron sputtering discharge: From plasma to structural and morphological analysis of layers, *Polymers* 12 (2020) 1–14, <https://doi.org/10.3390/polym12123065>.
- [16] R. El Zrelli, L. Rabaoui, N. Daghbouj, H. Abda, S. Castet, C. Josse, P. van Beek, M. Souhail, S. Michel, N. Bejaoui, P. Courjault-Radé, Characterization of phosphate rock and phosphogypsum from Gabes phosphate fertilizer factories (SE Tunisia): high mining potential and implications for environmental protection, *Environ. Sci. Pollut. Res.* 25 (2018) 14690–14702, <https://doi.org/10.1007/s11356-018-1648-4>.
- [17] G.C. Gomes, F.F. Borghi, R.O. Ospina, E.O. López, F.O. Borges, A. Mello, Nd:YAG (532 nm) pulsed laser deposition produces crystalline hydroxyapatite thin coatings at room temperature, *Surf. Coat. Technol.* 329 (2017) 174–183, <https://doi.org/10.1016/j.surfcoat.2017.09.008>.
- [18] K. Grabas, A. Pawelecny, Z. W. Strek, E. Szleg, S. Strek, Study on the properties of waste apatite phosphogypsum as a raw material of prospective applications, *Waste Biomass.Valoriz.* 10 (2019) 3143–3155, <https://doi.org/10.1007/s12649-018-0316-8>.
- [19] S. Hajimirzaee, S. Chansai, C. Hardacre, C.E. Banks, A.M. Doyle, Effects of surfactant on morphology, chemical properties and catalytic activity of hydroxyapatite, *J. Solid State Chem.* 276 (2019) 345–351, <https://doi.org/10.1016/j.jssc.2019.05.031>.
- [20] E. Hasret, M. Ipekoglu, S. Altintas, N.A. Ipekoglu, Microwave-assisted synthesis of hydroxyapatite for the removal of lead(II) from aqueous solutions, *Environ. Sci. Pollut. Res.* 19 (2012) 2766–2775, <https://doi.org/10.1007/s11356-012-0776-5>.
- [21] N.S.N. Hasnan, M.A. Mohamed, N.A. Anuar, M.F. Abdul Sukur, S.F. Mohd Yusoff, W.N.A. Wan Mokhtar, Z.A. Mohd Hir, N.A. Mohd Shohaimi, H. Ahmad Rafiae, Emerging polymeric-based material with photocatalytic functionality for sustainable technologies, *J. Ind. Eng. Chem.* 113 (2022) 32–71, <https://doi.org/10.1016/j.jiec.2022.06.009>.
- [22] N.S.N. Hasnan, M.A. Mohamed, Z.A. Mohd Hir, Surface physicochemistry modification and structural nanoarchitectures of g-C₃N₄ for wastewater remediation and solar fuel generation, *Adv. Mater. Technol.* (2022), <https://doi.org/10.1002/admt.202100993>.
- [23] Y. Hong, Z. Fang, B. Yin, B. Luo, Y. Zhao, W. Shi, C. Li, A visible-light-driven heterojunction for enhanced photocatalytic water splitting over Ta₂O₅ modified g-C₃N₄ photocatalyst, *Int. J. Hydrog. Energy* 42 (2017) 6738–6745, <https://doi.org/10.1016/j.ijhydene.2016.12.055>.
- [24] H. Hou, X. Zhang, Rational design of 1D/2D heterostructured photocatalyst for energy and environmental applications, *Chem. Eng. J.* 395 (2020) 125030, <https://doi.org/10.1016/j.cej.2020.125030>.
- [25] F. Hubert, F. Testard, O. Spalla, Cetyltrimethylammonium bromide silver bromide complex as the capping agent of gold nanorods, *Langmuir* 24 (2008) 9219–9222, <https://doi.org/10.1021/la801711q>.
- [26] N.L. Ignjatović, L. Mancić, M. Vuković, Z. Stojanović, M.G. Nikolić, S. Škapin, S. Jovanović, L. Veselinović, V. Uskoković, S. Lazić, S. Marković, M.M. Lazarević, D.P. Uskoković, Rare-earth (Gd³⁺, Yb³⁺, Tm³⁺, Eu³⁺) co-doped hydroxyapatite as magnetic, up-conversion and down-conversion materials for multimodal, *Sci. Rep.* 9 (2019) 1630, <https://doi.org/10.1038/s41598-019-52885-0>.
- [27] M. Jarcho, C.H. Bolen, M.B. Thomas, J. Bobick, J.F. Kay, R.H. Doremus, Hydroxyapatite synthesis and characterization in dense polycrystalline form, *J. Mater. Sci.* 11 (1976) 2027–2035, <https://doi.org/10.1007/PL00020328>.
- [28] K.J. Joshi, N.M. Shah, Structural, morphological & optical studies of Hydroxyapatite microplates synthesized using hydrothermal technique, *Mater. Today Proc.* (2023), <https://doi.org/10.1016/j.matpr.2023.01.411>.
- [29] G.M.P. Jr, J.E. Gambe, E.M. Alcantara, R.M. Vequizo1, X-ray diffraction and infrared spectroscopy analyses on the crystallinity of engineered biological hydroxyapatite for medical application, *IOP Conf. Ser.: Mater. Sci. Eng.* 79 (2015) 012028, <https://doi.org/10.1088/1757-899X/79/1/012028>.
- [30] V.M. Kashkarov, D.L. Goloshchapov, A.N. Rumyantseva, P.V. Seredin, E. P. Domashhevskaya, I.A. Spivakova, B.R. Shumilovich, X-ray diffraction and IR spectroscopy investigation of synthesized and biogenic nanocrystalline hydroxyapatite, *J. Surf. Investigig.* 5 (2011) 1162–1167, <https://doi.org/10.1134/S1027451011120068>.
- [31] M. Khalid, M. Mujahid, S. Amin, R.S. Rawat, A. Nusair, G.R. Deen, Effect of surfactant and heat treatment on morphology, surface area and crystallinity in hydroxyapatite nanocrystals, *Ceram. Int.* 39 (2013) 39–50, <https://doi.org/10.1016/j.ceramint.2012.05.090>.
- [32] K. Kuperkar, L. Abezgauz, K. Prasad, P. Bahadur, Formation and growth of micelles in dilute aqueous CTAB solutions in the presence of NaNO₃ and NaClO₃, *J. Surfactants Deterg.* 13 (2010) 293–303, <https://doi.org/10.1007/s11743-009-1173-z>.
- [33] X. Lei, T. Xu, W. Yao, Q. Wu, R. Zou, Hollow hydroxyapatite microspheres modified by CdS nanoparticles for efficiently photocatalytic degradation of tetracycline, *J. Taiwan Inst. Chem. Eng.* 106 (2020) 148–158, <https://doi.org/10.1016/j.jtice.2019.10.023>.
- [34] J.A. Lett, S. Sagadevan, J.J. Prabhakar, N.A. Hamizi, I.A. Badruddin, M.R. Johan, A.R. Marlinda, Y.A. Wahab, T.M.Y. Khan, S. Kamangar, Drug leaching properties of Vancomycin loaded mesoporous hydroxyapatite as bone substitutes, *Processes* 7 (2019) 1–12, <https://doi.org/10.3390/pr7110826>.
- [35] Yan Li, Y. Li, Z.-X. Deng, J. Zhuang, X. Sun, Surfactant-assisted hydrothermal synthesis of hydroxyapatite nanopowders, *J. Nanosci. Nanotechnol.* 12 (2012) 8042–8049, <https://doi.org/10.1166/jnn.2012.6664>.
- [36] J. Lin, H. Yang, J. Zhang, S. Yang, G. Lu, Y. Zhang, H. Qin, J. Xi, L. Song, Surface restructuring Ni_{0.85}Se/ZnSe catalyst shows large boosting electrocatalytic and photoelectrochemical performance, *Ceram. Int.* 50 (2024) 6713–6724, <https://doi.org/10.1016/j.ceramint.2023.12.010>.
- [37] J. Lin, H. Yang, J. Zhang, S. Yang, G. Lu, Y. Zhang, J. Kong, L. Song, Electronic band structure adjustable NiS_xSe_{1-x} ternary catalysts show omnipotent boosting ability in photoelectrochemistry, electrocatalysis and photocatalysis, *Int. J. Hydrog. Energy* 56 (2024) 1475–1488, <https://doi.org/10.1016/j.ijhydene.2023.12.252>.
- [38] D. Li, X. Zhao, Q. Zhou, B. Ding, A. Zheng, Q. Peng, Z. Hou, Vicinal hydroxyl group-inspired selective oxidation of glycerol to glyceric acid on hydroxyapatite supported Pd catalyst, *Green. Energy Environ.* 7 (2022) 691–703, <https://doi.org/10.1016/j.gee.2020.11.018>.
- [39] X. Li, Z. Zhou, G. Zhao, Z. Liu, Utilization of phosphogypsum for backfilling, way to relieve its environmental impact, *Gospod. Surowcami Miner.* 24 (2008) 225–231.
- [40] Li Yan, Y. Li, Z.-X. Deng, J. Zhuang, X. Sun, Surfactant-assisted hydrothermal synthesis of hydroxyapatite nanopowders, *J. Nanosci. Nanotechnol.* 12 (2012) 8042–8049, <https://doi.org/10.1166/jnn.2012.6664>.
- [41] Y. Liu, Y.X. Yu, W.D. Zhang, Carbon quantum dots-doped CdS microspheres with enhanced photocatalytic performance, *J. Alloy. Compd.* 569 (2013) 102–110, <https://doi.org/10.1016/j.jallcom.2013.03.202>.
- [42] E.O. López, P.L. Bernardo, N.R. Checca, A.L. Rossi, A. Mello, D.E. Ellis, A.M. Rossi, J. Terra, Hydroxyapatite and lead-substituted hydroxyapatite near-surface structures: Novel modelling of photoemission lines from X-ray photoelectron spectra, *Appl. Surf. Sci.* 571 (2022), <https://doi.org/10.1016/j.apsusc.2021.151310>.
- [43] Y. Lv, Yanyan Zhu, Yongta Zhu, Enhanced photocatalytic performance for the BiPO₄-x nanorod induced by surface oxygen vacancy, *J. Phys. Chem. C* 117 (2013) 18520–18528, <https://doi.org/10.1021/jp405596e>.
- [44] N. Méndez-Lozano, R. Velázquez-Castillo, E.M. Rivera-Muñoz, L. Bucio-Galindo, G. Mondragón-Galicia, A. Manzano-Ramírez, M.Á. Ocampo, L.M. Apártiga-Castro, Crystal growth and structural analysis of hydroxyapatite nanofibers synthesized by the hydrothermal microwave-assisted method, *Ceram. Int.* 43 (2017) 451–457, <https://doi.org/10.1016/j.ceramint.2016.09.179>.
- [45] M.A. Mohamed, M.F. M. Zain, L. Jeffery Minggu, M.B. Kassim, J. Jaafar, N. Saidina Amin, Y.H. Ng, Revealing the role of kapok fibre as bio-template for In-situ construction of C-doped g-C₃N₄@C, N co-doped TiO₂ core-shell heterojunction photocatalyst and its photocatalytic hydrogen production performance, *Appl. Surf. Sci.* 476 (2019) 205–220, <https://doi.org/10.1016/j.apsusc.2019.01.080>.
- [46] M.A. Mohamed, M.F. M. Zain, L. Jeffery Minggu, M.B. Kassim, N.A. Saidina Amin, W.N. W. Salleh, M.N.I. Salehmin, M.F. Md Nasir, Z.A. Mohd Hir, Constructing bio-templated 3D porous microtubular C-doped g-C₃N₄ with tunable band structure and enhanced charge carrier separation, *Appl. Catal. B* 236 (2018) 265–279, <https://doi.org/10.1016/j.apcatb.2018.05.037>.
- [47] S.N.F. Moridon, K. Arifin, M.A. Mohamed, L.J. Minggu, R. Mohamad Yunus, M. B. Kassim, TiO₂ Nanotubes Decorated with Mo₂C for Enhanced Photoelectrochemical Water-Splitting Properties, *Materials* 16 (18) (2023) 6261, <https://doi.org/10.3390/ma16186261>.
- [48] N.K. Nga, L.T. Giang, T.Q. Huy, P.H. Viet, C. Migliaresi, Surfactant-assisted size control of hydroxyapatite nanorods for bone tissue engineering, *Colloids Surf. B Biointerfaces* 116 (2014) 666–673, <https://doi.org/10.1016/j.colsurfb.2013.11.001>.
- [49] E. Nimmy, P. Wilson, Investigations on sonofragmentation of hydroxyapatite crystals as a function of strontium incorporation, *Ultrason. Sonochem.* 50 (2019) 188–199, <https://doi.org/10.1016/j.ulsonch.2018.09.018>.
- [50] S.C. Oh, J. Xu, D.T. Tran, B. Liu, D. Liu, Effects of Controlled Crystalline Surface of Hydroxyapatite on Methane Oxidation Reactions, *ACS Catal.* 8 (2018) 4493–4507, <https://doi.org/10.1021/acscatal.7b04011>.

- [51] M. Othmani, H. Bachoua, Y. Ghandour, A. Aissa, M. Debbabi, Synthesis, characterization and catalytic properties of copper-substituted hydroxyapatite nanocrystals, *Mater. Res. Bull.* 97 (2018) 560–566, <https://doi.org/10.1016/j.materresbull.2017.09.056>.
- [52] D. Pham Minh, N.D. Tran, A. Nzihou, P. Sharrock, Carbonate-containing apatite (CAP) synthesis under moderate conditions starting from calcium carbonate and orthophosphoric acid, *Mater. Sci. Eng. C* 33 (2013) 2971–2980, <https://doi.org/10.1016/j.msec.2013.03.023>.
- [53] C.V. Reddy, R. Koutavarapu, R.V.S.S.N. Ravikumar, J. Shim, A novel green-emitting Ni^{2+} -doped Ca-Li hydroxyapatite nanopowders: structural, optical, and photoluminescence properties, *J. Mater. Sci.: Mater. Electron.* 31 (2020) 5097–5106, <https://doi.org/10.1007/s10854-020-03070-x>.
- [54] M.N.I. Salehmin, L. Jeffery Minggu, W.F. Mark-Lee, M.A. Mohamed, K. Arifin, M.H. H. Jumali, M.B. Kassim, Highly photoactive Cu_2O nanowire film prepared with modified scalable synthesis method for enhanced photoelectrochemical performance, *Sol. Energy Mater. Sol. Cells* 182 (2018) 237–245, <https://doi.org/10.1016/j.solmat.2018.03.042>.
- [55] K. Shu, C. Chuaicham, Y. Noguchi, L. Xu, K. Sasaki, In-situ hydrothermal synthesis of Fe-doped hydroxyapatite photocatalyst derived from converter slag toward xanthate photodegradation and Cr(VI) reduction under visible-light irradiation, *Chem. Eng. J.* 459 (2023), <https://doi.org/10.1016/j.cej.2023.141474>.
- [56] H.A. Siddiqui, K.L. Pickering, M.R. Micalo, A review on the use of hydroxyapatite-carbonaceous structure composites in bone replacement materials for strengthening purposes, *Materials* 11 (2018) 1–32, <https://doi.org/10.3390/ma110101813>.
- [57] Y. Slimani, M.A. Almessiere, S.E. Shirasath, E. Hannachi, G. Yasin, A. Baykal, B. Ozçelik, I. Ercan, Investigation of structural, morphological, optical, magnetic and dielectric properties of $(1-x)\text{BaTiO}_3/x\text{Sr}_{0.92}\text{Ca}_{0.04}\text{Mg}_{0.04}\text{Fe}_{12}\text{O}_{19}$ composites, *J. Magn. Magn. Mater.* 510 (2020) 166933, <https://doi.org/10.1016/j.jmmm.2020.166933>.
- [58] H. Tan, Z. Zhao, W. Zhu, Bin, E.N. Coker, B. Li, M. Zheng, W. Yu, H. Fan, Z. Sun, Oxygen vacancy enhanced photocatalytic activity of perovskite SrTiO_3 , *ACS Appl. Mater. Interfaces* 6 (2014) 19184–19190, <https://doi.org/10.1021/am5051907>.
- [59] M. Thommes, K. Kaneko, A.V. Neimark, J.P. Olivier, F. Rodriguez-Reinoso, J. Rouquerol, K.S.W. Sing, Physisorption of gases, with special reference to the evaluation of surface area and pore size distribution (IUPAC Technical Report), *Pure Appl. Chem.* 87 (2015) 1051–1069, <https://doi.org/10.1515/pac-2014-1117>.
- [60] U. Vijayalakshmi, S. Rajeswari, Influence of process parameters on the sol-gel synthesis of nano hydroxyapatite using various phosphorus precursors, *J. Solgel Sci. Technol.* 63 (2012) 45–55, <https://doi.org/10.1007/s10971-012-2762-2>.
- [61] M. Vukomanović, V. Žunić, M. Otonićar, U. Repnik, B. Turk, S.D. Škapin, D. Suvorov, Hydroxyapatite/platinum bio-photocatalyst: A biomaterial approach to self-cleaning, *J. Mater. Chem. B* 22 (2012) 10571–10580, <https://doi.org/10.1039/c2jm00136e>.
- [62] B. Wang, J.J. Zhang, Z.Y. Pan, X.Q. Tao, H.S. Wang, A novel hydrogen peroxide sensor based on the direct electron transfer of horseradish peroxidase immobilized on silica-hydroxyapatite hybrid film, *Biosens. Bioelectron.* 24 (2009) 1141–1145, <https://doi.org/10.1016/j.bios.2008.06.053>.
- [63] Y.J. Wang, J. Chen, Di, K. Wei, S.H. Zhang, X.D. Wang, Surfactant-assisted synthesis of hydroxyapatite particles, *Mater. Lett.* 60 (2006) 3227–3231, <https://doi.org/10.1016/j.matlet.2006.02.077>.
- [64] Z. Wei, Z. Deng, Research hotspots and trends of comprehensive utilization of phosphogypsum: Bibliometric analysis, *J. Environ. Radio.* 242 (2022) 106778, <https://doi.org/10.1016/j.jenvrad.2021.106778>.
- [65] Y.H. Xiao, C.Q. Xu, W.De Zhang, Facile synthesis of Ni-doped WO_3 nanoplate arrays for effective photoelectrochemical water splitting, *J. Solid State Electrochem.* 21 (2017) 3355–3364, <https://doi.org/10.1007/s10008-017-3680-6>.
- [66] H. Yang, Y. Wang, Morphology control of hydroxyapatite microcrystals: Synergistic effects of citrate and CTAB, *Mater. Sci. Eng. C* 62 (2016) 160–165, <https://doi.org/10.1016/j.msec.2016.01.052>.
- [67] Shuang Men Yan He, Charge distribution of phosphonium ionic liquids: phosphonium versus phosphate, *Russ. J. Phys. Chem. A* 94 (2020) 2091–2095, <https://doi.org/10.1134/S0036024420100131>.
- [68] M. Zargazi, M. Chahkandi, M. Baghayeri, New highly efficient 2D/1D HAp/g-C₃N₄ photocatalyst thin film insight into crystal orientation and C-vacancy effects, *Chemosphere* 303 (2022) 135079, <https://doi.org/10.1016/j.chemosphere.2022.135079>.
- [69] W. Zhang, Y. Chai, X. Xu, Y. Wang, N. Cao, Rod-shaped hydroxyapatite with mesoporous structure as drug carriers for proteins, *Appl. Surf. Sci.* 322 (2014) 71–77, <https://doi.org/10.1016/j.apsusc.2014.10.064>.
- [70] Y.F. Zhao, J. Ma, Triblock co-polymer templating synthesis of mesostructured hydroxyapatite, *Microporous Mesoporous Mater.* 87 (2005) 110–117, <https://doi.org/10.1016/j.micromeso.2005.07.046>.
- [71] H. Zhou, J. Lee, Nanoscale hydroxyapatite particles for bone tissue engineering, *Acta Biomater.* 7 (2011) 2769–2781, <https://doi.org/10.1016/j.actbio.2011.03.019>.